Electrically switching transverse modes in high power THz quantum cascade lasers

S. Fathololoumi[1, 2,*], E. Dupont[1], S. G. Razavipour[2], S. R. Laframboise[1], A. Delage[1], Z. R. Wasilewski[1], A. Bezinger[1], G. Z. Rafi[2], S. Safavi-Naeini[2], D. Ban[2], and H.C. Liu[1]

[1] *Institute for Microstructural Sciences, National Research Council of Canada, 1200 Montreal Road, Ottawa, ON, K1A0R6, Canada*

[2] *Department of Electrical and Computer Engineering, University of Waterloo, 200 University Ave W., Waterloo, ON, N2L3G1, Canada*

* *sfatholo@ece.uwaterloo.ca*

Abstract: The design and fabrication of a high power THz quantum cascade laser (QCL), with electrically controllable transverse mode is presented. The switching of the beam pattern results in dynamic beam switching using a symmetric side current injection scheme. The angular-resolved L-I curves measurements, near-field and far-field patterns and angular-resolved lasing spectra are presented. The measurement results confirm that the quasi-TM_{01} transverse mode lases first and dominates the lasing operation at lower current injection, while the quasi-TM_{00} mode lases at a higher threshold current density and becomes dominant at high current injection. The near-field and far-field measurements confirm that the lasing THz beam is maneuvered by 25° in emission angle, when the current density changes from 1.9 kA/cm^2 to 2.3 kA/cm^2. A two-dimension (2D) current and mode calculation provides a simple model to explain the behavior of each mode under different bias conditions.

OCIS codes: (140.5965) Semiconductor lasers, quantum cascade; (140.3295) Laser beam characterization.

References and links

1. S. Kumar, Q. Hu, and J. L. Reno, "186 K operation of terahertz quantum-cascade lasers based on a diagonal design," Appl. Phys. Lett. **94**(13), 131105 (2009).
2. E. E. Orlova, J. N. Hovenier, T. O. Klaassen, I. Kasalynas, A. J. L. Adam, J. R. Gao, T. M. Klapwijk, B. S. Williams, S. Kumar, Q. Hu, and J. L. Reno, "Antenna model for wire lasers," Phys. Rev. Lett. **96**(17), 173904 (2006).
3. M. Tonouchi, "Cutting-edge terahertz technology," Nat. Photonics **1**(2), 97–105 (2007).
4. S. Kumar, B. S. Williams, Q. Qin, A. M. Lee, Q. Hu, and J. L. Reno, "Surface-emitting distributed feedback terahertz quantum-cascade lasers in metal-metal waveguides," Opt. Express **15**(1), 113 (2007).
5. E. Mujagić, C. Deutsch, H. Detz, P. Klang, M. Nobile, A. M. Andrews, W. Schrenk, K. Unterrainer, and G. Strasser, "Vertically emitting terahertz quantum cascade ring lasers," Appl. Phys. Lett. **95**(1), 011120 (2009).
6. Y. Chassagneux, R. Colombelli, W. Maineults, S. Barbieri, S. P. Khanna, E. H. Linfield, and A. G. Davies, "Predictable surface emission patterns in terahertz photonic-crystal quantum cascade lasers," Opt. Express **17**(12), 9491–9502 (2009).
7. M. I. Amanti, M. Fischer, C. Walther, G. Scalari, and J. Faist, "Horn antennas for terahertz quantum cascade lasers," Electron. Lett. **43**(10), 573 (2007).
8. J. Lloyd-Hughes, G. Scalari, A. van Kolck, M. Fischer, M. Beck, and J. Faist, "Coupling terahertz radiation between sub-wavelength metal-metal waveguides and free space using monolithically integrated horn antennae," Opt. Express **17**(20), 18387–18393 (2009).
9. A. Wei Min Lee, Q. Qin, S. Kumar, B. S. Williams, Q. Hu, and J. L. Reno, "High-power and high-temperature THz quantum-cascade lasers based on lens-coupled metal-metal waveguides," Opt. Lett. **32**(19), 2840–2842 (2007).
10. N. Yu, J. Fan, Q. J. Wang, C. Pflugl, L. Diehl, T. Edamura, M. Yamanishi, H. Kan, and F. Capasso, "Small-divergence semiconductor lasers by plasmonic collimation," Nat. Photonics **2**(9), 564–570 (2008).
11. A. A. Danylov, J. Waldman, T. M. Goyette, A. J. Gatesman, R. H. Giles, K. J. Linden, W. R. Neal, W. E. Nixon, M. C. Wanke, and J. L. Reno, "Transformation of the multimode terahertz quantum cascade laser beam into a Gaussian, using a hollow dielectric waveguide," Appl. Opt. **46**(22), 5051–5055 (2007).
12. M. I. Amanti, M. Fischer, G. Scalari, M. Beck, and J. Faist, "Low-divergence single-mode terahertz quantum cascade laser," Nat. Photonics **3**(10), 586–590 (2009).

#126283 - $15.00 USD Received 30 Mar 2010; revised 20 Apr 2010; accepted 25 Apr 2010; published 28 Apr 2010

13. M. Hajenius, P. Khosropanah, J. N. Hovenier, J. R. Gao, T. M. Klapwijk, S. Barbieri, S. Dhillon, P. Filloux, C. Sirtori, D. A. Ritchie, and H. E. Beere, "Surface plasmon quantum cascade lasers as terahertz local oscillators," Opt. Lett. **33**(4), 312–314 (2008).
14. H. Luo, S. R. Laframboise, Z. R. Wasilewski, G. C. Aers, H. C. Liu, and J. C. Cao, "Terahertz quantum-cascade lasers based on a three-well active module," Appl. Phys. Lett. **90**(4), 041112 (2007).
15. S. Fathololoumi, D. Ban, H. Luo, E. Dupont, S. R. Laframboise, A. Boucherif, and H. C. Liu, "Thermal Behavior Investigation of Terahertz Quantum-Cascade Lasers," IEEE J. Quantum Electron. **44**(12), 1139–1144 (2008).
16. S. Fathololoumi, E. Dupont, D. Ban, M. Graf, S. R. Laframboise, Z. R. Wasilewski, and H. C. Liu, "Time resolved thermal quenching of THz quantum cascade lasers," IEEE J. Quantum Electron. **46**(3), 396–404 (2010).
17. E. Dupont, S. Fathololoumi, and H. C. Liu, "Simplified density matrix model applied to three-well terahertz quantum cascade lasers," Accepted in Phys. Rev. B (2010).
18. G. Scalari, R. Terazzi, M. Giovannini, N. Hoyler, and J. Faist, "Population inversion by resonant tunneling in quantum wells," Appl. Phys. Lett. **91**(3), 032103 (2007).
19. N. Yu, L. Diehl, E. Cubukcu, C. Pflügl, D. Bour, S. Corzine, J. Zhu, G. Höfler, K. B. Crozier, and F. Capasso, "Near-field imaging of quantum cascade laser transverse modes," Opt. Express **15**(20), 13227–13235 (2007).
20. P. Gellie, W. Maineult, A. Andronico, G. Leo, C. Sirtori, S. Barbieri, Y. Chassagneux, J. R. Coudevylle, R. Colombelli, S. P. Khanna, E. H. Linfield, and A. G. Davies, "Effect of transverse mode structure on the far field pattern of metal-metal terahertz quantum cascade lasers," J. Appl. Phys. **104**(12), 124513 (2008).
21. M. I. Amanti, C. Walther, M. Fischer, N. Hoyler, L. Sirigu, G. Scalari, and J. Faist, "Study and improvement of THz quantum cascade laser beam-pattern for different waveguides configurations,", The Ninth International Conference on Intersubband Transitions in Quantum Wells (ITQW 2007), 2007, http://www.itqw07.leeds.ac.uk/abs/M_I_Amanti_Study_and_improvement.pdf.
22. S. Kohen, B. S. Williams, and Q. Hu, "Electromagnetic modeling of terahertz quantum cascade laser waveguides and resonators," J. Appl. Phys. **97**(5), 053106 (2005).
23. S. L. Chuang, "Physics of optoelectronic devices," John Wiley and sons Inc: New York (1995).
24. J. T. Robinson, K. Preston, O. Painter, and M. Lipson, "First-principle derivation of gain in high-index-contrast waveguides," Opt. Express **16**(21), 16659–16669 (2008).
25. A. Lyakh, P. Zory, D. Wasserman, G. Shu, C. Gmachl, M. D'Souza, D. Botez, and D. Bour, "Narrow stripe-width, low-ridge high power quantum cascade lasers," Appl. Phys. Lett. **90**(14), 141107 (2007).

1. Introduction

After roughly a decade of intense research on terahertz (THz) quantum cascade lasers (QCL), the prototype devices are getting closer to be deployed for various THz applications [1]. Due to sub-wavelength dimension of the laser structure, the emission pattern of the device is inherently diffractive (wide-angle beam) [2]. Focused and controllable emission beam profiles are crucial for many applications [3]. Engineering the laser emission beam pattern is demonstrated using grating [4,5], photonic crystals [6] and external mode converters such as horn antennas [7,8], Si lenses [9], plasmonics [10] and hollow dielectric waveguides [11]. The THz beam with a divergence angle as low as eight degrees has been recently reported by employing a third order grating on a ridge waveguide [12]. Although the beam shape of the laser has been engineered and steered using different designs of photonic crystal structures, dynamically controllable beam emission from a single THz QCL has not been achieved yet. In this work we report the bias-controlled tuning of the emission direction of a THz QCL. Beam switching is achieved by selectively exciting different waveguide transverse modes under different current injection schemes.

We focus our study on a Semi-Insulating Surface Plasmon (SI-SP) based THz QCL. In this structure the optical mode profile extends to the semi-insulating substrate and hence is not tightly confined in the active region. The device shows relatively less divergent emission patterns and also higher output power at the expense of higher optical loss [13]. The top contact is a metal layer directly on the top of the ridge waveguide and the bottom contacts consist of two Au metal layers besides the ridge waveguide, sitting on a 400 nm thick n^+ GaAs layer which is underneath the QCL active region (see Fig. 1). The substrate is electrically insulating, the current is therefore laterally injected into the quantum-well active region from both sides of the laser ridge through the thin bottom n^+ GaAs layer. The side current injection leads to laterally non-uniform distribution of the injected current and electrical potential, giving rise to a laterally non-uniform gain profile. The local gain profile, even though non-uniform, is laterally symmetric due to current injection equally from both sides of the ridge. The lateral non-uniformity of the gain profile plays an important role in deciding which transverse mode can be excited, because of the different extent to which the transverse modes overlap with the gain profile. As a result, quasi-TM_{00} or quasi-TM_{01} may be selectively

#126283 - $15.00 USD Received 30 Mar 2010; revised 20 Apr 2010; accepted 25 Apr 2010; published 28 Apr 2010

excited under different current injection. For simplicity from now on, we call these quasi-TM modes as TM mode. In this work, we present the experimental and theoretical results of the near-field and far-field patterns from a SI-SP THz QCL under different current injection. Our results demonstrate that controllable beam switching can be achieved by selectively exciting different transverse modes of the devices. We also present a simplified model of the modal gain that qualitatively explains why the fundamental mode TM_{00} lases later than TM_{01} and becomes dominant at high current.

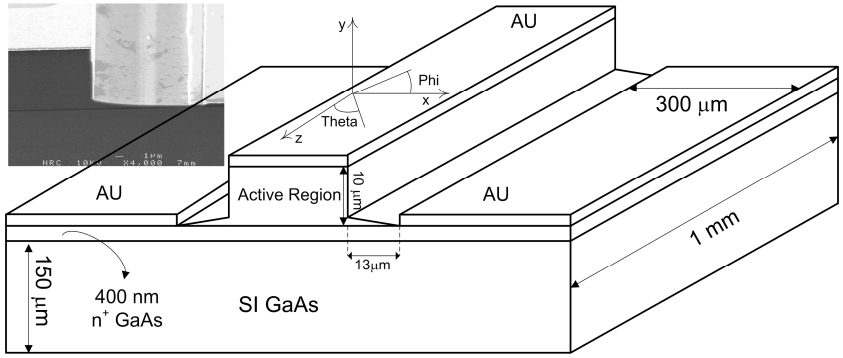

Fig. 1. Schematic presentation of the THz QCL structure: The Au contacts on the sides are 13 μm away form each side of the ridge. Definition of the angles for far-field measurement and simulation is shown in the graph. The inset shows the SEM micrograph of the fabricated 150 μm wide laser ridge.

2. Fabrication

The cascade module of the THz QCL used in this study consists of three quantum wells (GaAs) and three barrier layers ($Al_{0.15}Ga_{0.85}As$), which is the same as the one reported in [14]. The layer thicknesses are **48**/ 96/ **20**/ 74/ **42**/ 161 Å, where the barriers are indicated in bold fonts. The quantum well of 161 Å is doped with Si dopants to a two-dimensional carrier concentration of 3.6×10^{10} cm^{-2}. The whole QCL structure consists of 216 repeats of this module in sandwich between a 50 nm top and 400 nm bottom n^+ GaAs layers doped to 5×10^{18} cm^{-3} and 3×10^{18} cm^{-3}, respectively. The whole structure is grown on a semi-insulating (SI) GaAs substrate by molecular beam epitaxy. THz wave is generated by a radiative transition between a pair of anti-crossed double-well states. Depopulation of lower lasing state is mediated by coupling to a wide and doped subsequent well, the longitudinal-optical (LO) phonon relaxation and the injection to the following module.

A sufficient wide ridge waveguide is needed to accommodate TM_{01} lateral mode. We selected 150 μm wide ridges for this purpose. With this ridge width, loss of TM_{00} and TM_{01} are comparable and are lower than TM_{02} mode loss. The ridge waveguide structure of the surface plasmon THz QCL device is fabricated using a dry etching process. The ridge waveguide is etched down to roughly ~10 μm in depth, which allows the exposure of the 400 nm thick n^+ GaAs layer for depositing the bottom contacts. The dry etch is targeted to stop at the boundary of active region and n^+ region. Metal layers of Pd/Ge/Ti/Pt/Au (55/100/25/50/300 nm) is deposited for the top contact (on top of the ridge) and the bottom contacts (on both sides of the ridge). The bottom contacts are 13 μm away from the edges of the ridge on both sides, respectively, to yield efficient and laterally symmetrical current injection. The SI GaAs substrate of the samples is then thinned down to 150 μm to facilitate heat dissipation from the active region to a heat sink underneath [15]. The sample is cleaved into laser bars with a ~1 mm long Fabry-Perot resonator. The laser bars are indium soldered (epi-layer side up) onto an oxygen-free copper package, wire bonded to the top and both sides of the ridge and then mounted in a closed-cycle Helium cryostat for measurements [16].

#126283 - $15.00 USD Received 30 Mar 2010; revised 20 Apr 2010; accepted 25 Apr 2010; published 28 Apr 2010

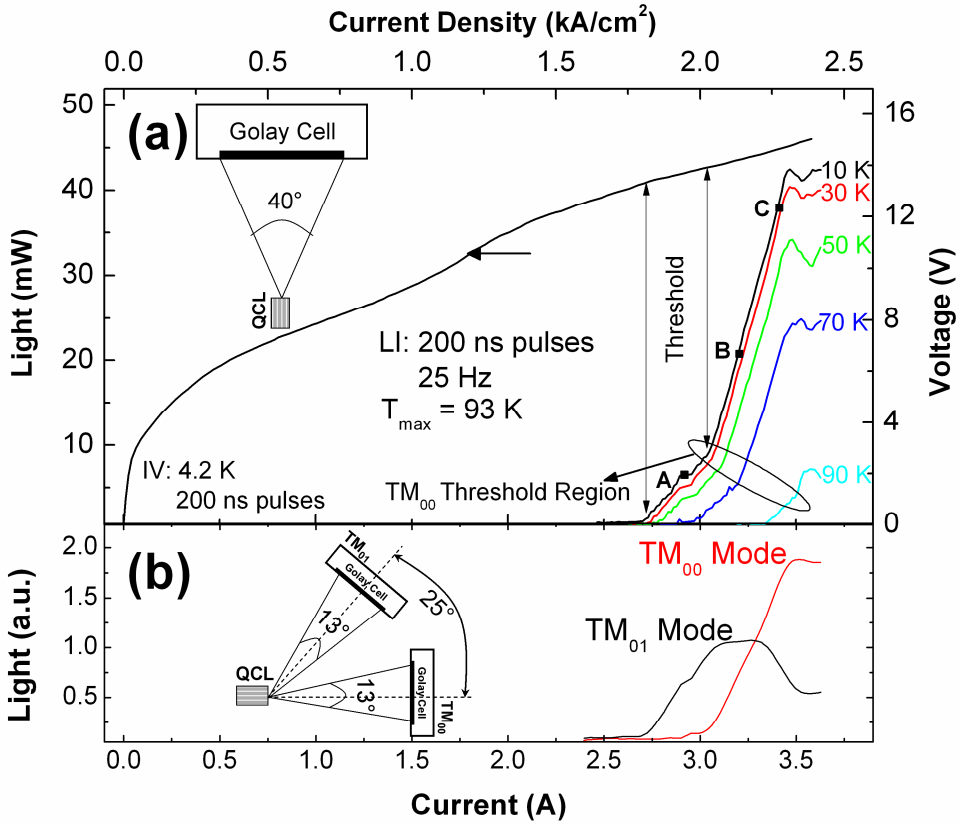

Fig. 2. (a) The collected THz light (optical output power) versus current curves for a 150 μm wide and 1 mm long THz QCL at different heat sink temperatures. The device is biased in pulsed mode (pulse width = 200 ns and repetition rate = 25 Hz). The IV characteristic is measured at 4.2 K using 200 ns pulses. The light is collected within a 40° emission cone. The slope change in L-I curve is attributed to the change of the mode excited inside the laser ridge waveguide. Lasing is observed up to a maximum temperature of 93 K. The horizontal arrow highlights the transparency current on V-I curve. (b) The collected THz light versus current curves for each mode. The TM_{00} is collected directly in front of the facet and the TM_{01} is collected by moving the detector off the normal direction by 25°. The collection cone in each case is 13°.

3. Results and discussions

Figure 2(a) shows the light-current (L-I) and voltage-current (V-I) characteristics of the QCL device in pulsed operation (with a 25 Hz repetition rate and a 200 ns pulse width) and under different heat-sink temperatures ranging from 10 K to 90 K. The V-I plot is measured using a four point technique, in which the four contact points are on the device to and side metal contact pads. The Golay cell detector collects 40° cone of the output THz light. The inset of Fig. 2(a) shows light collection scheme. The laser device starts to lase at J_{th} = 1.83 kA/cm^2 (13.4 V), at 10 K. As the current density further increases to ~2.0 kA/cm^2 (13.9 V), the L-I curve shows a kink – an increase in slope efficiency. This L-I kink at 2.0 kA/cm^2 is not related to the alignment of subbands between neighboring cascade modules, because no significant kinks are observed in the voltage-current (V-I) curve in the corresponding current density region. The slope kink is consistently observed in the L-I curves at temperatures ranging from 10 K to 90K. As will be revealed by further experimental and theoretical studies, the two distinct slopes in the L-I curves are attributed to the excitation of two different transverse modes (TM_{00} and TM_{01}) in the laser device. The kink in the V-I curve at $V \approx 10$ V and $J \approx 1.2$ kA/cm^2 is due to the indirect coupling of the injector state with the collector state, where the

#126283 - $15.00 USD Received 30 Mar 2010; revised 20 Apr 2010; accepted 25 Apr 2010; published 28 Apr 2010

transparency condition is approximately reached [highlighted by horizontal arrow in Fig. 2(a)] [17].

An iris is then used to confine THz emission inside a collection cone with a solid-angle of 13°. This experiment measures angular-resolved L-I curve, with a confined collection cone angle. Figure 2(b) shows two L-I curves measured at 10 K along two different emission directions. The TM_{00} mode curve is measured along the normal direction of the laser facet and the TM_{01} mode curve is measured at an angle of 25° off the normal direction [see the inset of Fig. 2(b)]. The two L-I curves show different threshold current density. The TM_{01} mode curve has a threshold current density of 1.83 kA/cm^2, which is the same as the one of the non-angular-resolved L-I curve in Fig. 2(a). The TM_{00} mode curve has a higher threshold current density of ~2.0 kA/cm^2, matching the current density at which the kink is observed in the non-angular-resolved L-I curve in Fig. 2(a).

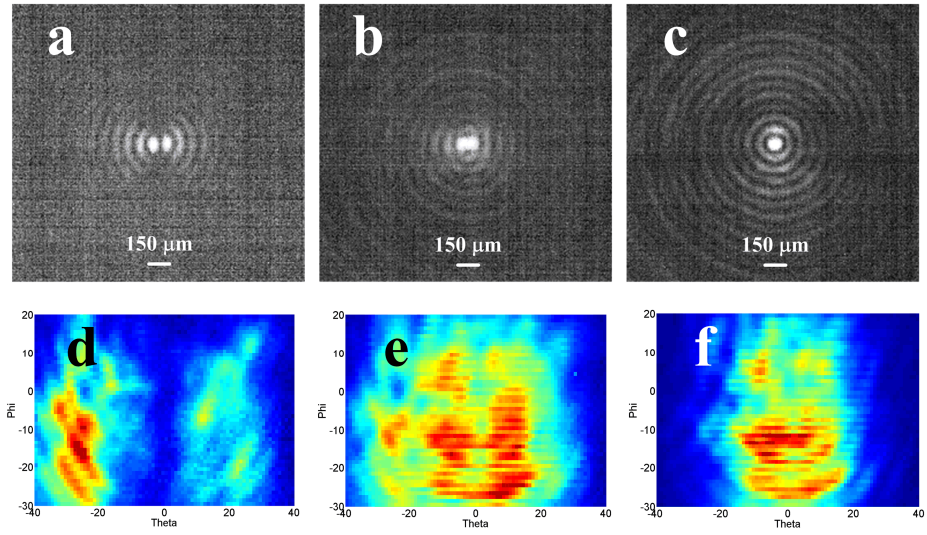

Fig. 3. (a)–(c) Near-field image of the 150 μm THz QCL ridge at different current injection levels (a- 2.9 A, b- 3.2 A, and c- 3.4 A). At lower current levels the clearly visible two lobes confirm the existence of only the TM_{01} mode (a). By increasing the current the fundamental mode catches up (b) until at very high current mainly the TM_{00} mode is excited (c). d-f) Far-field measurement results of the THz QCL at various current levels (d- 2.9 A, e- 3.2 A, and f- 3.4 A). At lower current level (I = 2.9 A), when only the TM_{01} mode is excited the beam pattern emits to angles beyond 20° (d). At I = 3.2 A by exciting the fundamental mode, the normal direction of the far-field is filled up (e). Further increase of the current up to I = 3.4 A leaves mainly the fundamental mode operating and the far-field beam pattern is focused within angles of ± 20°.

The observed change of THz emission direction suggests different transverse modes are excited when the device is biased at different currents [19,20]. To confirm this hypothesis of transverse mode change, we use a FLIR Photon 640 micro-bolometer camera to capture the near-field emission pattern at the laser facet. The original lens of the camera is replaced by a Tsurupica lens with 80% transparency at the lasing wavelength. A biconvex spherical lens with a focal length of 50 mm and diameter of 45 mm was chosen for this experiment. The lens tube is purged using dry nitrogen in order to minimize atmospheric vapor absorption. By ignoring spherical aberration, the spatial resolution of the optical system, as defined by diffraction, is already 150 μm. Therefore, the shape of the modal field cannot be well resolved. The recorded images are dominated by diffraction effect of the lens (at the origin of the concentric rings). For high order modes the image is dominated by interferences between the different sections of the opposite signed field. Despite the fact the optical setup could be further improved, for convenience we call these images as “near-field”; they are useful to qualitatively identify the excited lateral modes. The near-field pattern images at the laser facet

#126283 - $15.00 USD Received 30 Mar 2010; revised 20 Apr 2010; accepted 25 Apr 2010; published 28 Apr 2010

are captured with a 2.5 time magnification (numerical aperture of 0.64). Figure 3(a) to 3(c) shows the near-field pattern measurement under different current injections (a: I = 2.9 A; b: I = 3.2 A; and c: I = 3.4 A), corresponding to the A, B, C points, labeled in the L-I curve in Fig. 2(a).

Figure 3(a) shows clearly that the transverse mode at the laser facet at (I = 2.9 A, point A) has two lobes (~90 μm apart), indicating a TM_{01} mode is excited in the waveguide. On the contrary, Fig. 3(c) (I = 3.4 A, point C) shows only one strong lobe at the center of the ridge, which is assigned to a TM_{00} mode. As for the intermediate current injection at I = 3.2 A (point B), the observed near-field pattern appears as the combination of the TM_{01} and TM_{00} modes. The measured near-field patterns show with no doubt that the different transverse modes are excited at different current injections. The TM_{01} mode is first excited at a lower current, while the TM_{00} mode (the fundamental mode) is excited at a higher current. The TM_{01} and TM_{00} modes can co-exist at an intermediate current injection.

The far-field emission pattern is the direct Fourier transform of the corresponding transverse modes at the laser emission facet. The two lobes in the TM_{01} mode are theoretically supposed to have opposite phase [19]. The two opposite-phase lobes of the TM_{01} mode should lead to destructive interference along the normal direction of the laser facet ($\phi = 0°$ and $\theta = 0°$, as defined in Fig. 1) at far-field, which can be verified by experimentally measuring the far-field emission patterns of the device. The results are shown in Fig. 3(d) to 3(f). As expected at a lower injection current (I = 2.9 A) when only the TM_{01} mode is excited, the far-field beam pattern [Fig. 3(d)] shows a minimum along the normal direction of the laser facet ($\theta = 0°$). The laser emission is diverged to off-normal directions at angles of $\theta = \pm 25°$ and beyond, respectively. This suggests that two lobes of TM_{01} mode have opposite phase and are located approximately $\lambda/2\sin\theta \approx 94\mu m$ apart. The non-symmetric far-field pattern might be caused by packaging asymmetry, where non-similar environment exists on each side of the waveguide facet. Along the vertical direction (ϕ) the far-field beam pattern is mainly distributed under the active region junction plane ($\phi < 0$), same as [21]. This is because a big portion of the transverse mode extends from the active region into the underneath semi-insulating substrate. When the device is biased at 3.4 A, only the fundamental mode TM_{00} is excited. Correspondingly, the far-field patter is mainly focused at the angle of $\theta = 0°$ [Fig. 3(f)]. At the intermediate current injection level (I = 3.2 A) when both TM_{00} and TM_{01} co-exist, the far-field beam pattern [Fig. 3(e)] displays combined features, as shown in Fig. 3(d) and 3(f).

Angular-resolved lasing spectra of the device at 10 K measured at the aforementioned three injection current levels once again reveal that two different transverse modes are excited. The spectra are measured along two different directions: $\theta = 0°$ and $\theta = 25°$ along which the TM_{00} and TM_{01} modes are found to radiate strongest, respectively. The two sets of spectra (in total 6) are shown in Fig. 4. All spectra are normalized to unity in peak intensity. The two spectra at I = 2.9 A ($\theta = 0°$ and $\theta = 25°$) have a main peak at 124.3 cm^{-1} and a much weaker Fabry-Perot (FP) side mode at 121.8 cm^{-1}. The FP longitudinal wavelengths are given by [23]

$$\lambda_m = \frac{2nL}{m}, \tag{1}$$

where n is the effective refractive index of the transverse mode, L the cavity length and m the FP mode number. The free spectral range (FSR) of the FP modes is hence 1.25 cm^{-1}. The two normalized spectra [Fig. 4(a)] looks similar to each other, while the absolute power at $\theta = 0°$ is much weaker than that at $\theta = 25°$. The two lasing peaks at 124.3 and 121.8 cm^{-1} belong to the same longitudinal Fabry-Perot mode family of the TM_{01} transverse mode. As the current rises to I = 3.2 A, a new peak at 120.9 cm^{-1} appears in both angular-resolved spectra [Fig. 4(b)]. The wave number difference between this new peak and the peak at 124.3 cm^{-1} is 3.4 cm^{-1}, which is not an integer product of the TM_{01} FP mode spacing (1.25 cm^{-1}). Apparently, they do not belong to the same FP longitudinal mode family. The lasing emission

#126283 - $15.00 USD Received 30 Mar 2010; revised 20 Apr 2010; accepted 25 Apr 2010; published 28 Apr 2010

at 120.9 cm^{-1} has the main peak at θ = 0° direction, while it is much weaker at θ = 25°, indicating that this lasing wavelength is from the TM_{00} transverse mode. The peak at 124.3 cm^{-1} of the TM_{01} mode dominates at θ = 25°, while is very weak but still observable at θ = 0° direction. The spectrum measurement result again confirms the co-existence of TM_{00} and TM_{01} modes at this current injection level (I = 3.2 A). The different FP longitudinal wavelengths of the TM_{00} and TM_{01} modes are attributed to slightly different effective refractive indices of these two transverse modes. With further increasing the current to 3.4 A, the peak at 120.9 cm^{-1} dominates at both θ = 0° and θ = 25° directions. The peak at 124.3 cm^{-1} disappears at θ = 0°, however, it is still observable at θ = 25°. The lasing spectra show that even at I = 3.4 A, both TM_{00} and TM_{01} are excited in the laser waveguide, nevertheless the TM_{00} is dominant. The results of the angular-resolved lasing spectra agree with the earlier observation of the near-field and far-field patterns.

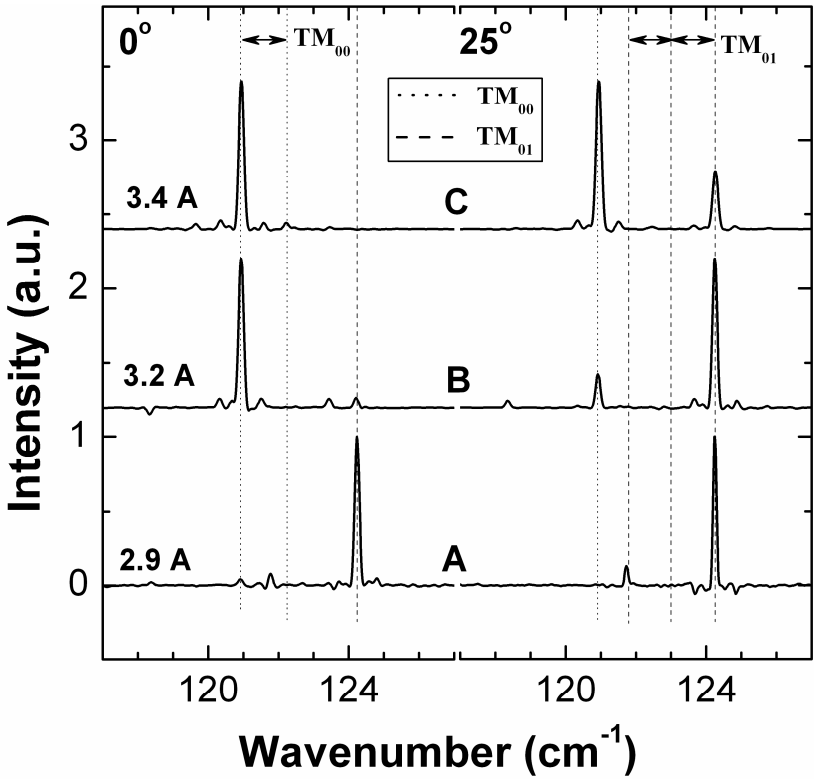

Fig. 4. Lasing spectra of the THz QCL at 10 K for various injection currents measured at 0° and 25° angles. Two families of Fabry-Perot modes are identified with the equal spacing (double-end arrows). By increasing the injection current the TM_{01} mode diminishes and the TM_{00} mode emerges. The resolution of the spectra is 0.1 cm^{-1}.

4. Simulation of far-field pattern

To confirm that the experimental observations of the far-field pattern measurements are really due to the excitation of the TM_{00} and TM_{01} modes, the HFSS (Finite Element Method) simulation software is employed to calculate the far-field beam patterns from the 3D model of ridge waveguide structure as depicted in Fig. 1. HFSS was used as a 3-D Driven-Modal solver. The first two modes of SI-SP waveguide were separately calculated by an embedded 2-D eigenmode solver. These two modes were then separately used to excite one facet of the laser structure. Exact truncation boundary conditions were considered for the other facets. As compared to most published analyses based on simplifying assumptions, in this work, the far

#126283 - $15.00 USD Received 30 Mar 2010; revised 20 Apr 2010; accepted 25 Apr 2010; published 28 Apr 2010

radiation fields are rigorously calculated from the modal field distributions over the entire 1 mm length of the structure. The conductivity of the contact metal and n^+ GaAs layers is calculated using Drude model with relaxation times of 60 fs and 100 fs, respectively [22]. The active region is modeled as a 10 μm thick GaAs layer with a background doping concentration of 8.15×10^{15} cm^{-3} and a Drude relaxation time of 500 fs. Despite the considerable computational complexity due to large mesh size and multi-resolution nature of the structure for the 3D simulation, the full length of the laser ridge (1 mm) is used in the accurate simulation of the fringes [2]. Figure 5(a) shows the simulated far-field pattern of the TM_{00} mode. The laser beam is mainly focused in an emission cone around $\theta = 0°$ and $\varphi = -10°$ direction, which agrees well with the experimental results shown in Fig. 3(f). Figure 5(b) shows the simulated far-field pattern of TM_{01} mode. The multiple-ring pattern of the simulated results resembles the experimental observation, whereas the experimental result [Fig. 3(d)] only shows the central-most ring due to the angular limit of the experimental setup collection cone. The simulation results confirm that the excited modes in the laser waveguide are TM_{00} and TM_{01} modes.

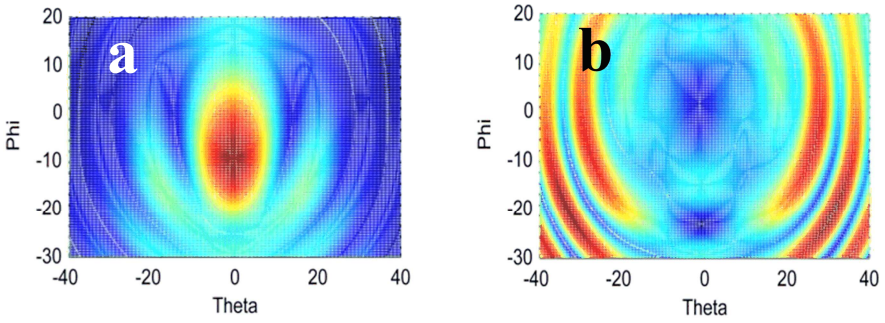

Fig. 5. HFSS simulation results for the far-field of the THz QCL depicted in Fig. 1 for (a) the TM_{00} and (b) the TM_{01} modes. The radiation wavelength for each mode is read from Fig. 4.

5. Simplified modal gain model

As mentioned before, the laser ridge is sufficiently wide (w = 150 μm) to support multiple transverse modes. However, among these, the particular transverse mode, which is excited, is the one with sufficient optical modal gain G_{ij} [23,24] given by,,

$$G_{ij} = \int_{AR} M_{ij}(x,y)\, g(x,y)\, dxdy, \tag{2a}$$

$$M_{ij}(x,y) = \frac{\mathrm{Re}\left(E_{ij}(x,y) \times H_{ij}^{*}(x,y)\right) \cdot \hat{z}}{\int_{Total} \mathrm{Re}\left(E_{ij}(x,y) \times H_{ij}^{*}(x,y)\right) \cdot \hat{z}\, dxdy}, \tag{2b}$$

where x *and* y are along the transverse directions, z is along the propagation direction (as shown in Fig. 1), $E_{ij}(x,y)$ and $H_{ij}(x,y)$ are the lateral electric and magnetic field profile of the ij^{th} transverse mode respectively, $M(x,y)$ is the normalized 2D mode power density, and $g(x,y)$ is the local non-uniform gain. Equations (2a) and (2b) assume the gain is proportional to the fraction of power that overlaps with the gain medium. As pointed out by Robinson et. *al.* in [24], this is correct for TM or quasi-TM modes, as long as the lateral confinement of the mode is not too strong. Because the SI-SP modes are mostly confined in the substrate, Eq. (2b) results in less than 2% error.

In order to calculate the 2D non-uniform gain profile, $g(x,y)$, we start from calculating voltage and current distribution by solving the 2D Poisson's equation as

#126283 - $15.00 USD Received 30 Mar 2010; revised 20 Apr 2010; accepted 25 Apr 2010; published 28 Apr 2010

$$\frac{\partial}{\partial x}\left(\sigma_x \frac{\partial V}{\partial x}\right)+\frac{\partial}{\partial y}\left(\sigma_y \frac{\partial V}{\partial y}\right)=0, \quad (3)$$

where σ_x and σ_y are lateral and vertical conductivities, respectively. We assume isotropic conductivity for all the regions, except the active region. For the n^+ GaAs region we used $\sigma_x = \sigma_y = 96000\ (\Omega.m)^{-1}$, which are given by Hall mobility measurement. The lateral conductivity of the active region (σ_x) is calculated using the weighted average of the bulk conductivities of GaAs and $Al_{0.15}Ga_{0.85}As$, with the given average doping [25]. The vertical conductivity of active region (σ_y) depends on the applied vertical electric field (E_y) [25]. To measure the vertical conductivity of the active region, it is required to conduct a four point measurement of the V-I curve of a device (preferably a non-lasing device), in which current is injected and flows vertically. For this purpose, a fabricated THz QCL with a metal-metal waveguide structure and the same active region material is employed. In such a structure, the current flows vertically through the active region from the top metal contact to the bottom metal contact without lateral spreading. As the current simulation results will be eventually used to calculate the gain, it is important to use the V-I of a non-lasing device to derive the conductivity. For this purpose, we fabricated a small micro-disc and cleaved it in half. Such a structure is expected to show very high waveguide loss, and hence destroy or strongly damp the lasing; nevertheless we observed very weak lasing form it. The vertical conductivity of the active region material is derived form measured V-I curve of this device. The final vertical conductivity used for the active region is in form of

$$\sigma_y = f(E_y). \quad (4)$$

The inset of Fig. 6 shows the measured DC vertical conductivity of the active region versus vertical electric field. We used COMSOL simulator to solve the Eq. (3) and calculate the current spreading at various applied voltages, for the 2D structure shown in Fig. 1. Figure 6 shows the lateral distribution of the vertical current, J_y, under different applied voltages, across the middle of the active region (5 μm below the top of the ridge). Two dashed lines show the corresponding current density levels, at which the TM_{01} and TM_{00} modes reach the lasing threshold (Fig. 2). Due to the bottom current injection configuration of the laser device, the lateral current density distribution, $J_y(x)$, is not uniform. As observed in Fig. 6, $J_y(x)$ is maximum at the two lateral edges of the ridge and is minimum at the center. The inset of Fig. 6 also compares the measured V-I curve shown in Fig. 2(a) with the simulated one. The simulated current agrees with the measurement results with a less than 1.5% mean square error.

In order to link the simulated current density to the local gain distribution, $g(x,y)$, it is required to estimate the intrinsic gain of the active material versus the vertical current density. To do so, we started from the L-I characteristic of a metal-metal THz QCL, where the current distribution in the active region is uniform. The threshold gain for such a device is estimated to be 40 cm^{-1} [17]. It is also shown in [17] that the transparency current density occurs after the alignment of the injection and collector states. The alignment is indicated by the bump in Fig. 2(a) V-I (horizontal arrow). For the gain material under study, the transparency current density (J_{tr}) is ~1.2 kA/cm^2. Assuming the Lorentzian gain model for the THz QCL active region, the gain becomes proportional to the population inversion (Δn). If the leakage tunneling time from the upper lasing state to the excited state of the phonon well, called wrong extraction channel, is much larger than the upper lasing state lifetime, the current efficiency for population inversion, Δn/J, is weakly dependent on the electric field, and therefore, population inversion increases linearly with current. For the sake of simplicity, we used such a linear approximation between the transparency point and threshold, even though we have demonstrated theoretically that the shunting effect by the wrong extraction channel cannot be neglected in our three-well design with vertical transitions [17]. Above the threshold, we assumed the emitted power is proportional to ($\Delta n/\ \Delta n_{th}$-1), where Δn is the population inversion if no photon were present in the cavity, and Δn_{th} is the population

#126283 - $15.00 USD Received 30 Mar 2010; revised 20 Apr 2010; accepted 25 Apr 2010; published 28 Apr 2010

inversion at threshold. Even though not strictly correct according to our ballistic model [17], this last approximation is reasonable.

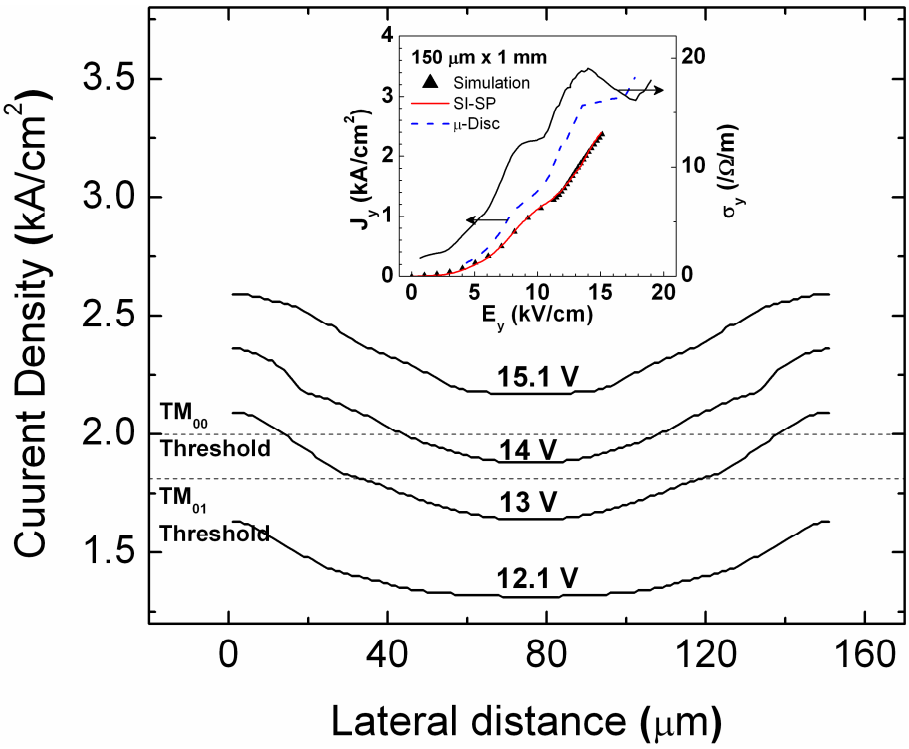

Fig. 6. Simulated vertical current density (J_y) profile at four different applied voltages (12.1, 13, 14, and 15.1 V). The current density profile is plotted though a cross section that is 5 μm below the top of the ridge. The two dashed lines show the corresponding current density at threshold for TM_{01} and TM_{00} modes. The inset shows the measured vertical conductivity of the active region versus the vertical electric field as measured from a metal-metal ridge laser. This curve is used in simulating the non-uniform 2D current profile. The inset also compares the simulated vertical current density with the experimental current in Fig. 2(a), and current of the micro-disc used to calculate the conductivity. The simulated V-I curve agrees with the experimental results with a less than 1.5% mean square error.

By applying all of above assumptions and combining with the measured L-I curve, the intrinsic gain versus current density is extracted and shown in Fig. 7. This curve is used to calculate the 2D local gain distribution at various applied voltages, in combination with simulated 2D current density profile. For current densities below 2 kA/cm^2, at which $g(x,y) \propto (J_y(x,y) - J_{tr})$, the local gain distribution, $g(x,y)$, has a similar lateral profile as that of $J_y(x,y)$. At higher current densities (>2.5 kA/cm^2) and below the negative differential resistance of the laser, the local gain diminishes probably due to the different detuning at the injection and extraction sides [18]. Since TM_{00} and TM_{01} modes have different distribution profile along the lateral direction of the device ridge, they overlap with the laterally non-uniform material gain profile to different extents, leading to different modal gains of these two modes. By controlling the current injection, one can favor one modal gain, while hold up the other one. As a result, the TM_{00} and TM_{01} modes can be selectively turned on under different biases.

In the last step, we simulate the 2D mode profile for each mode, as defined in Eq. (2b). The inset of Fig. 8 shows the simulated mode profile in the active region for the TM_{00} and TM_{01} modes, using the COMSOL simulator. These two mode distributions are inserted into the Eq. (2a), together with the calculated voltage dependant non-uniform local gain distribution to calculate the total reserve of gain. Each mode (TM_{ij}) reaches the threshold

#126283 - $15.00 USD Received 30 Mar 2010; revised 20 Apr 2010; accepted 25 Apr 2010; published 28 Apr 2010

when the reserve of gain increases up to the total modal loss ($\alpha_{tot\text{-}ij} = \alpha_{m\text{-}ij} + \alpha_{w\text{-}ij}$). We call such a figure of merit the net modal gain of the material and define it as

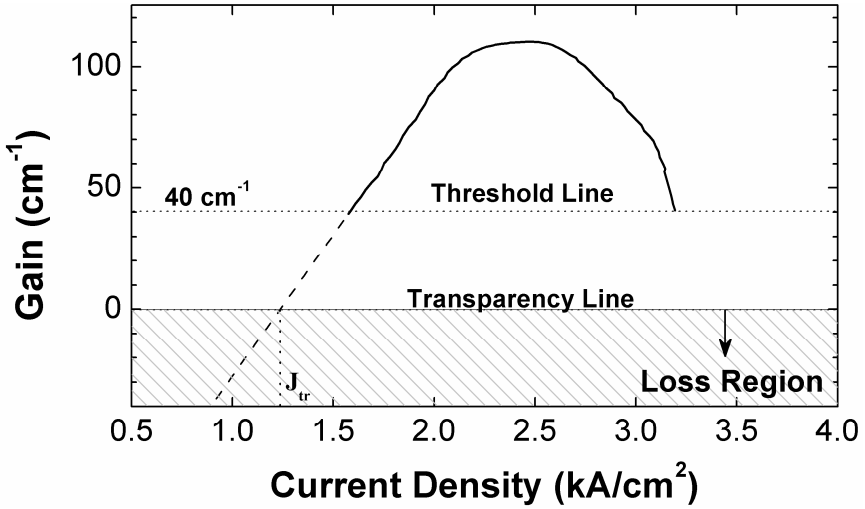

Fig. 7. Estimated intrinsic gain of the active region versus current density for three well LO-phonon based THz QCL active region. The curve is extracted from the L-I characteristic of a metal-metal device that is made of the same active region material. The negative differential resistance of this device is at 3.15 kA/cm^2.The curve is employed to calculate the net modal gain of the TM_{00} and TM_{01} modes.

$$G_{ij-net} = \int_{AR} M_{ij}(x,y)g(x,y)dxdy - \alpha_{tot-ij}. \quad (5)$$

To estimate the waveguide loss for each mode, we use the imaginary parts of corresponding effective index from the eigenmode solution of the Maxwell's equation. The modal mirror loss (α_m) is directly related to the modal reflectivity at the laser facet, which depends on the modal index and angle. A good approximation of the modal reflectivity is obtained by decomposing the main component of the electric field in a series plane waves by 2D Fourier transform. The coefficient of each of these waves is multiplied by the Fresnel reflection coefficient applied separately for contributions parallel and perpendicular to the plane of incidence. The total reflected field is then reconstructed by inverse Fourier transform; and the reflectivity is estimated by averaging the ratio of the reflected field intensity over the incident field. The mirror loss and the waveguide loss for different modes are, therefore, given by $\alpha_m = \ln(R)/L$ and $\alpha_w = 2\beta \times 2\pi/\lambda$, where R is the calculated reflectivity and β is the imaginary part of the propagation constant [19]. Table 1 lists the calculated modal waveguide and mirror loss values. Lower mirror loss of TM_{01} can be explained using ray optics approach for a polarization perpendicular to the plane of incidence; the higher order mode impinges on the facet at a larger incident angle and hence is more reflective [19]. Lower waveguide loss of TM_{01} mode originates from smaller overlap of this mode with the active region and the n^+ layer underneath it.

Table 1. Calculated modal waveguide and mirror loss values in cm^{-1}

	α_m	α_w	$\alpha_{tot} = \alpha_m + \alpha_w$
TM_{00}	9.67	5.31	14.98
TM_{01}	7.76	4.00	11.76

#126283 - $15.00 USD Received 30 Mar 2010; revised 20 Apr 2010; accepted 25 Apr 2010; published 28 Apr 2010

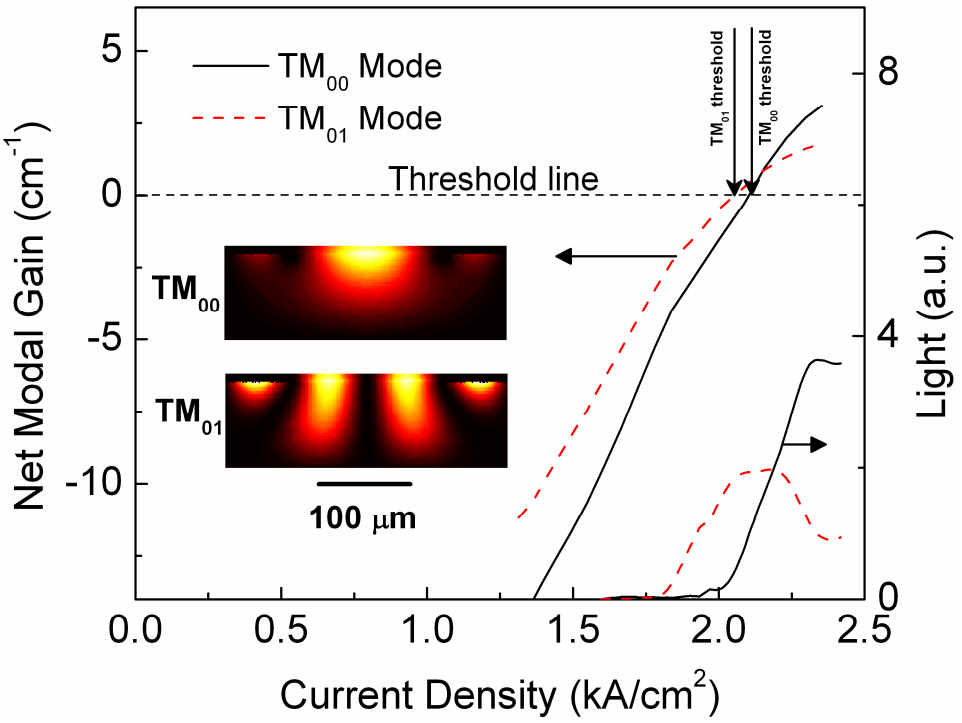

Fig. 8. Net model gain versus different applied voltage, calculated for the TM_{01} and TM_{00} modes. The TM_{01} mode reaches the threshold around the voltage of 2.04 kA/cm^2 (13.95 V). TM_{00} mode reaches the threshold around the voltage of 2.11 kA/cm^2 (14.13 V). The arrows show the threshold for each mode. The right axis re-plots the modal light curve versus voltage, from Fig. 2, to compare the simulated modal threshold with the experiments. The inset shows the 2D mode profiles of the TM_{00} and TM_{01} modes. The two main opposite phase lobes of TM_{01} are 85 μm apart.

Figure 8 shows the calculated net gain versus applied voltage for each mode. When the device is biased at a lower bias (lower current injection), the gain profile has maxima near the edges of the waveguide, which spatially overlaps more with the TM_{01} mode than with the TM_{00} mode. As a result, the TM_{01} mode possesses higher net gain than the TM_{00} mode and reaches the lasing threshold first. This explains why the experimental results show that the TM_{01} mode has a lower simulated threshold current density of J_{th} = 2.04 kA/cm^2 (compared to experimental value of J_{th} = 1.83 kA/cm^2) and starts to lase first. As the current injection continues to increase, the local gain in the center part of the ridge increases, which contributes more to the modal gain of the TM_{00} mode and brings it to the threshold point. According to this simplified model, the TM_{00} mode starts to lase at J_{th} = 2.11 kA/cm^2 which is close to experimental (J_{th} = 2 kA/cm^2). Further increase of the current injection renders the local current density at the lateral edges of the waveguide to exceed the maximum current density – beyond which the quantum wells become absorptive rather than emissive. Consequently, the net modal gain of the TM_{01} mode degrades and the lasing emission from the TM_{01} mode saturates. The TM_{00} mode is less affected by this gain-reduction process, because the maxima for lateral distribution of the current (on the edges) and TM_{00} mode profile (on the center) do not overlap. As observed in Fig. 2(a), the TM_{00} mode dominates at a current injection of J = 2.25 kA/cm^2 (V ≈14.5 V), which is also consistent with the simulated graph in Fig. 8. The discrepancy between the simulated and the measured J_{th} for each mode can be attributed to various sources of error such as, underestimation of the total loss (particularly for TM_{01} mode) and the estimated intrinsic gain of the active region, etc.

#126283 - $15.00 USD Received 30 Mar 2010; revised 20 Apr 2010; accepted 25 Apr 2010; published 28 Apr 2010

6. Conclusions

We designed and fabricated a high power THz QCL, which exhibits electrically controllable dynamic beam switching using a symmetric side current injection scheme. The angular-resolved L-I curves measurements, near-field and far-field patterns and angular-resolved lasing spectra all confirm that the TM_{01} transverse mode lases first and dominates the lasing operation at lower current injection, while the TM_{00} mode lases at a higher threshold current density and becomes dominant at high current injection. Because of the different near-field patterns at the laser emission facet of the TM_{00} and TM_{01} transverse modes, the far-field of the laser shows two lobes of radiation at horizontal angles of $\theta = \pm 25°$ when operating in TM_{01} mode under lower current injection and single lobe radiation at $\theta = 0°$ when operating in TM_{00} mode under higher current injection. The THz emission beam of the device can be easily and dynamically maneuvered by switching the applied device bias. The experimental results are in qualitatively reasonable agreement with the results of the simplified model of the modal gain.

#126283 - $15.00 USD Received 30 Mar 2010; revised 20 Apr 2010; accepted 25 Apr 2010; published 28 Apr 2010